INSTITUTE OF PHYSICS PUBLISHING PLASMA SOURCES SCIENCE AND TECHNOLOGY
Plasma Sources Sci. Technol. **16** (2007) 13–22 doi:10.1088/0963-0252/16/1/003

A calibrated infrared imaging study on the steady state thermal behaviour of Hall effect thrusters

S Mazouffre[1,3], P Echegut[2] and M Dudeck[1]

[1] Laboratoire d'Aérothermique, 1C Avenue de la Recherche Scientifique, 45071 Orléans, France
[2] CRMHT, 1D Avenue de la Recherche Scientifique, 45071 Orléans, France

E-mail: stephane.mazouffre@cnrs-orleans.fr

Received 21 June 2006, in final form 27 September 2006
Published 31 October 2006
Online at stacks.iop.org/PSST/16/13

Abstract
The thermal behaviour of Hall effect thrusters was investigated by means of calibrated infrared thermal imaging performed in the 8–9 μm spectral domain. Study on the variation of the steady state temperature of Hall thruster elements like discharge chamber (channel) walls and anodes along with discharge voltage and propellant (xenon) mass flow rate confirms that energy loss mechanisms, which are responsible for the heating of the thrusters, are a direct consequence of interactions between charged particles and surfaces. In order to obtain new insights into plasma surface interactions inside a thruster, the channel wall temperature was monitored over a broad range of electrical power stretching from 400 W to 5.5 kW for three types of thrusters with different designs, dimensions and operation domains, namely SPT100-ML, PPS ® 1350-G and PPSX000-ML. Note that over the range of thruster operating conditions the facility backpressure varies from 10^{-5} to 6×10^{-5} mbar. In addition, the effect of discharge chamber wall material on temperature field was also investigated using dielectric BN–SiO_2 and AlN walls as well as conducting graphite walls. For a given thruster geometry and material, a simple relationship between the mean wall temperature and the input electrical power can be established, in contradiction to the complex dynamics of such a magnetized plasma medium. Besides, thruster thermal history and degree of wear do not have a strong impact on power losses inside the channel.

1. Introduction

Electric propulsion is nowadays considered a very promising concept for space applications [1, 2]. Among all proposed electric propulsive devices such as the arcjet, magneto plasma dynamic thruster, gridded ion engine and Hall effect thruster (HET), the latter is currently recognized as an attractive propulsion means for maneouvres that require a large velocity change. HETs, also called stationary plasma thrusters or closed electron drift thrusters, are advanced propulsion devices that use an electric discharge to ionize and accelerate a propellant gas [3, 4]. Due to interesting features in terms of propellant ejection speed, efficiency, flexibility and lifetime, HETs are now employed for missions like geo-stationary satellite orbit correction and station keeping. The additional utilization of high power Hall thrusters for orbit transfer would also offer significant benefits in terms of launch mass, payload mass and operational life. Moreover, HETs appear as good candidates to be used as the primary propulsion engine for space probes during interplanetary journeys, as confirmed by the successful SMART-1 Moon flyby solar-powered mission of the European Space Agency [5].

The basic physics of a HET consists of a magnetic barrier in a low pressure dc discharge generated between an external hollow cathode and an anode [3, 6, 7]. The anode, which also serves as a gas injector, is located at the upstream end of a

[3] Author to whom any correspondence should be addressed.

coaxial annular dielectric channel that confines the discharge. Xenon is generally used as a propellant gas for its specific properties in terms of high atomic mass and low ionization energy. A set of solenoids provides a radially directed magnetic field $\boldsymbol{B}$ of which the strength is maximum in the vicinity of the channel exhaust. The magnetic field is chosen strong enough to make the electron Larmor radius much smaller than the discharge chamber length but weak enough not to affect ion trajectories. The electric potential drop is mostly concentrated in the final section of the channel owing to the low electron axial mobility in this restricted area. The corresponding induced local axial electric field $\boldsymbol{E}$ has two main effects. First it drives a high electron azimuthal drift—the so-called Hall current—that is responsible for the efficient ionization of the supplied gas. Second, it accelerates the ions to very high speed, which generates thrust and creates a plasma plume. The ion beam is neutralized by a fraction of electrons emitted from the hollow cathode. When operating near 1.3 kW, a HET ejects ions at 20 km s^{-1} and generates 80 mN of thrust with an overall efficiency of about 50%.

The thermal state of a Hall effect thruster, which mainly results from power losses onto the discharge chamber wall surface, determines to a large extent the channel wall properties such as secondary electron production and erosion rate. Therefore, the temperature field greatly influences thruster performances and efficiency [8]. Moreover, thermal stress endured by a thruster during ignition and shut down stages, and the subsequent material embrittlement, certainly influences the thruster lifetime. From a technological viewpoint, accurate knowledge about the overall thermal load experienced by a HET during operation is critical for radiator and magnetic circuit design purposes, lifetime prediction and running cycle definition. The acquisition of reliable data about the temperature field of thruster elements, especially the discharge chamber walls, and energy loss mechanisms therefore appears to be of crucial relevance for existing thruster optimization and for the development of high power dual-mode HETs [9].

In most experimental works dedicated to thermal characterization of HETs, the temperature of various thruster components was determined by means of thermocouples [8, 10]. Thermocouples embedded in the thruster structure provide a standard means of temperature determination, however severe plasma conditions encountered in the discharge chamber and the plasma plume as well as access restriction greatly complicate the measurement process. Another way to estimate temperature fields in a HET consists of employing a radiative–conductive thermal model [10, 11]. However, such a method relies on an estimate of the overall thruster energy balance in terms of distribution of energy between physical processes involved in thrust generation.

Thermal imaging is first a qualitative diagnostic technique that permits us to obtain relative temperature change during thruster thermal cycles as well as when varying working parameters. Nevertheless, the present state of commercially available technology makes infrared imaging a quantitative diagnostic provided that the emissivity of the viewed area is known. To the best of our knowledge, thermal imaging has so far solely been applied to acquire infrared images of gridded ion engines [12]. In this contribution, we present results that concern the measurement of HET temperature fields by means of calibrated thermal imaging. The steady state thermal behaviour of several thrusters was examined in a broad range of applied electrical power: a laboratory version of the Russian SPT100 thruster [4], named SPT100-ML, the PPS®1350-G Hall thruster developed by Snecma [13], which equips the SMART-1 lunar orbiter, and the high power PPSX000-ML thruster [9]. In particular the study aimed at a better understanding of the effect of thruster design and geometry as well as channel wall material upon energy loss mechanisms at work inside the discharge chamber of a Hall effect thruster.

2. Basic concepts

2.1. Equations of thermal radiation

The radiation theory is based on Planck's radiation law that relates the number of photons per unit volume per unit wavelength-interval, emitted by a blackbody, i.e. an integral radiator, to the temperature of the latter [14, 15]. The overall power M^{bb} radiated into a hemisphere by a blackbody is obtained from integration of Plancks law over the entire spectral domain. The M^{bb} quantity is often referred to as the blackbody radiant exitance or emissive power, and it reads

$$M^{\mathrm{bb}} = \sigma T^4 \qquad \text{in W m}^{-2}, \tag{1}$$

where σ is the so-called Stefan–Boltzmann constant[4] and T is the blackbody absolute temperature in K. For blackbodies, Lambert's law holds exactly. Thus, the power radiated by a blackbody surface S at temperature T into a hemisphere is

$$Q = M^{\mathrm{bb}}(T)\, S = \sigma\, T^4\, S \qquad \text{in W}. \tag{2}$$

The spectral emissivity ε is defined as the ratio of the emissive power of a given body to that of a blackbody within a narrow spectral interval. The temperature must be alike for the two bodies. Thus the spectral emissivity is given by

$$\varepsilon(\lambda, T) = \frac{M_\lambda(\lambda, T)}{M_\lambda^{\mathrm{bb}}(\lambda, T)}, \tag{3}$$

where λ is the wavelength. A material which has an emissivity that is independent of wavelength is called a grey body.

The integration of equation (3) over the entire spectral band leads to the well-known Stefan–Boltzmann's relation, which relates the thermodynamic temperature of a body to the total photon flux M emitted by the latter:

$$M(T) = \varepsilon(T)\, \sigma\, T^4 \qquad \text{in W m}^{-2}. \tag{4}$$

Thus, measurement of the total radiation emitted from a body allows us to determine the temperature of its surface, provided that ε is known for the temperature of interest. Infrared detectors are only able to capture radiations over a well-defined short wavelength range $\Delta\lambda$. Hence, the Stefan–Boltzmann law cannot be directly applied to determine the temperature from the recorded photon flux magnitude. Instead, equation (3) must be integrated within $\Delta\lambda = \lambda_2 - \lambda_1$, to obtain a relation between

[4] $\sigma = 5.6704 \times 10^{-8}$ W m^{-2} K^{-4}

the detected radiation power $M_{\Delta\lambda}$ and the temperature. This yields

$$M_{\Delta\lambda}(T) = \int_{\Delta\lambda} \varepsilon(\lambda, T) M_{\lambda}^{bb}(\lambda, T)\, d\lambda, \\ = \overline{\varepsilon}(T)\, F(\lambda_1, \lambda_2, T)\, \sigma T^4, \quad (5)$$

where $\overline{\varepsilon}(T)$ is the average spectral emissivity within the spectral domain $\Delta\lambda$. An analytical solution for equation (5) cannot be found if the bandwidth is finite, i.e. the F function can solely be computed numerically [14]. If well over half of the power is radiated within the $\Delta\lambda$ interval, however, Stefan–Boltzmann's law is a good approximation. In our case, due to the camera sensitivity in the far infrared and a narrow detection bandwidth, Stefan–Boltzmann's formula cannot be employed and one must turn towards equation (5). Note that the latter reveals that the photon flux received by an infrared photodetector does not exactly vary as T^4.

Thermal imaging consists of determining the temperature of a surface by measuring the radiation flux that originates from the latter. The obtained temperature is correct if, within the probed spectral range, reflexion of incident radiations from the surface and transmission through the surface can both be neglected. In that case the measured flux solely depends on the surface temperature and it is given by equation (5) [15]. In the remainder of the paper we consider that emission of infrared radiations is the dominant process for all surfaces whatever the material they are made of.

2.2. *Spectral emissivity measurement*

In order to enable absolute temperature determination for the thruster discharge chamber walls, which also act as thermal insulators, the spectral emissivity of material they are made of was measured in air as a function of temperature. The measurements were performed with an upgraded fast Fourier transform spectrometer Bruker IFS 113v of which specific features are given in [16]. The evolution of the normal emissivity of fresh BN–SiO_2 and AlN pieces is displayed in figure 1 for different temperatures. Within the 8–9 μm spectral band probed by the infrared camera, the emissivity does not change much with temperature. The mean emissivity is given in table 1 for the three materials used in this work. The emissivity of a given sample depends not only upon wavelength and temperature as previously mentioned but also upon viewing angle, material composition and surface conditions like roughness and oxidation level. As a consequence, the emissivity of thermal insulators can vary in the course of thruster operation owing to wear and subsequent change in geometry as well as coating formation. For that reason, the emissivity of a BN–SiO_2 ring has been assessed from IR measurements after several tens of hours of thruster operation[5]. No significant change in emissivity value was noticed despite an obvious surface modification. Such an outcome was expected as the measurement spectral domain lies in the vicinity of Christiansen's wavelength for which each dielectric compound acts as a blackbody. Note that in view of its specific properties in terms of secondary electron generation, sputtering yield, thermal and mechanical features, BN–SiO_2 is currently employed as HET wall material [4].

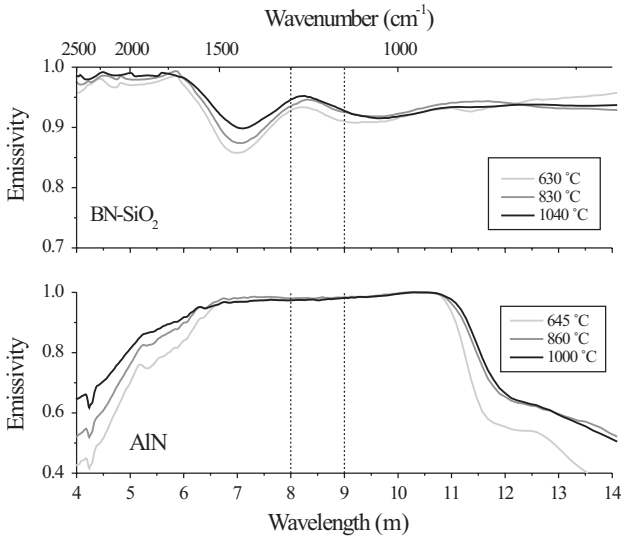

Figure 1. BN–SiO_2 and AlN normal emissivity as a function of wavelength for different temperatures. The mean emissivity in the 8–9 μm band is equal to 0.92 and 0.98, respectively, for BN–SiO_2 and AlN.

Table 1. Normal spectral emissivity in the 8–9 μm domain of various HET channel wall materials.

BN–SiO_2	AlN	Graphite
0.92	0.98	0.56

The emissivity of a stainless steel sample ε_{SS} depends drastically on the exact steel composition as well as on surface state and thermal history. According to handbooks, ε_{SS} varies between 0.3 and 0.9. Moreover, ε_{SS} depends strongly upon the observation angle. To be able to assess the temperature of the thruster anode, the emissivity of the latter was inferred from thermal imaging while keeping the thruster at room temperature. The emissivity was found to be in the 0.7–0.9 range. A value of 0.8 will be used for ε_{SS} in the following chapters.

3. IR camera and experimental arrangement

Hall effect thruster infrared image acquisition has been accomplished with a computer controlled calibrated infrared camera ThermaCAM^{TM}SC 3000 manufactured by FLIR systems [17]. The infrared camera is equipped with a GaAs quantum well infrared photodetector (QWIP) that consists of a set of 320 × 240 pixels. The QWIP is Stirling cooled down to −200 °C to reduce the camera intrinsic noise. The detector is suited for the 8–9 μm spectral domain. An overall temperature range from −20 to 1500 °C is covered by automatically adjusting an internal shutter. A camera frame rate up to 750 Hz is available, which allows to perform time-resolved infrared measurements. On the basis of the energy conservation equation, a characteristic time scale can be determined for both conductive (τ_c) and radiative (τ_r) heat transfer phenomena [18]. For a BN–SiO_2 compound, one finds $\tau_c = 8$ s and $\tau_r = 0.3$ s

[5] The ceramic ring was kept at a constant temperature while performing thermal imaging with the calibrated camera.

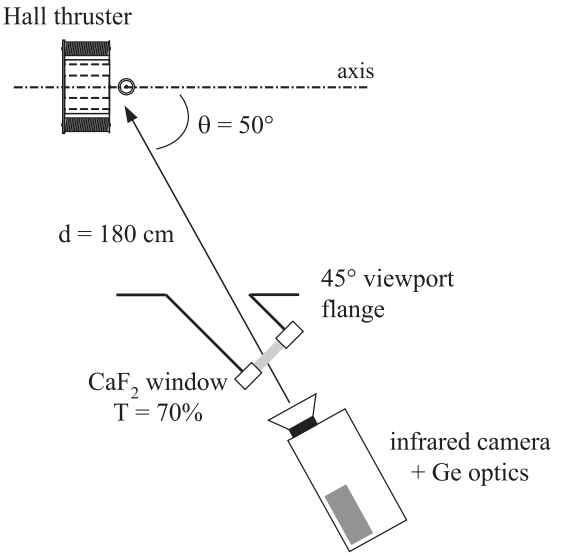

Figure 2. Drawing of the experimental arrangement used for infrared thermal imaging of Hall effect thrusters in the PIVOINE ground-test facility.

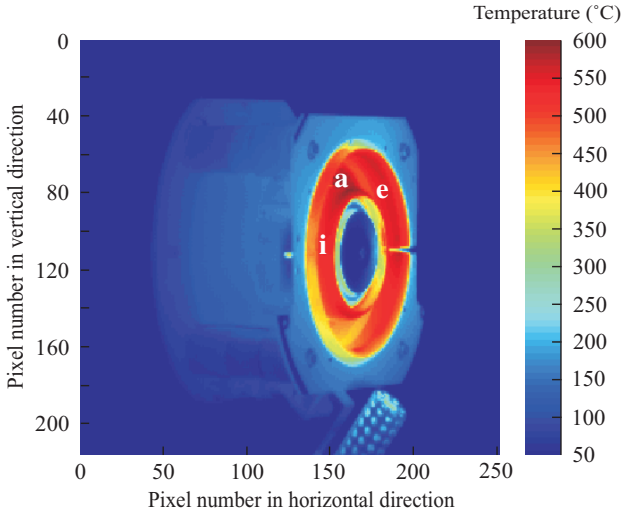

Figure 3. Calibrated infrared image of a SPT100-ML Hall effect thruster equipped with BN–SiO_2 channel walls ($\varepsilon = 0.92$). The input electrical power is 1260 W. Also shown are the probed zones location: e → external channel wall, i → internal channel wall, a → anode.

(This figure is in colour only in the electronic version)

at 800 K. The majority of images was acquired with a frame rate of 50 Hz.

All experiments were conducted in the PIVOINE ground-test facility [4]. A sketch of the experimental arrangement is depicted in figure 2. The infrared camera was located at a distance of 180 cm from the HET front plate. The thruster observation angle was 50°, in which case the camera viewed virtually the entire thruster. Observation was carried out through a 10 mm in thickness CaF_2 window with a 70% transition in the 8–9 μm IR band. The transmission coefficient was measured with a FTIR spectrometer. In order to improve the image resolution of thruster components, magnified images were produced with the use of Ge optics with 10 and 7° numerical apertures in horizontal and vertical directions, respectively.

A calibrated infrared image of the SPT100-ML thruster taken with the camera while running under standard conditions is shown in figure 3. The SPT100-ML thruster operates nominally with a total xenon mass flow rate $\dot{m}_{Xe} = 5.42\,\mathrm{mg\,s^{-1}}$, an applied voltage $U_d = 300$ V and a discharge current $I_d \approx 4.5$ A. In figure 3 the emissivity is fixed to 0.92, i.e. the temperature field is solely correct for the discharge chamber ceramic walls. The inner and outer thermal insulators, which sustained the power dissipated by the plasma, together with the anode/gas distributor, which collects the discharge current, are clearly the most intense infrared sources in the image. Thermograms obtained with the infrared camera are treated with a specific software in such a way that every single pixel element can be analysed separately [19]. The error in the measured temperature mostly arises from two parameters, i.e. the material spectral emissivity and the CaF_2 window IR light transmission coefficient. An average value of ε is used over the 8–9 μm domain. The CaF_2 transmission slightly varies in the course of a measurement campaign due to coating formation. A statistical analysis indicates that error in the wall temperature is below ±4%. In the case of the anode the error is ±10% at the most. Also shown in figure 3 are the zones of which the thermal behaviour is monitored during thruster operation. Zone e, respectively i, corresponds to the outer ceramic channel wall, respectively the inner wall. Note that these two temperatures are measured in the final section of the thermal insulators. This region, through which magnetic and electric fields are strong, corresponds to the ion acceleration zone [3, 6]. The area labelled a corresponds to the anode.

All thermograms examined in this work have been acquired in thermal steady state. After ignition—the plasma creation time is below 1 μs [20, 21]—the inner and outer channel walls and anode temperature rises rapidly. Subsequently, other thruster elements like body, magnetic circuit and coil housing heat up due to heat transfer by conduction and radiation [19]. The characteristic time for thermal transient process differs depending on the thruster component. In the case of a SPT100 type thruster under nominal conditions, it takes about 50 min for the insulators and the anode to reach thermal equilibrium whereas it takes about 2 h for thruster body [19].

During experiments, the facility background gas pressure varies from 10^{-5} to 6×10^{-5} mbar as the xenon mass flow rate is changed from 3 to 11 $\mathrm{mg\,s^{-1}}$.

4. Steady state temperature of a Hall effect thruster

4.1. Plasma–surface interaction inside the channel

The thrust efficiency is given by

$$\eta_F = \frac{F^2}{2\dot{m}_{Xe}(U_d I_d + P_{coils})}, \tag{6}$$

where F is the thrust, $\dot{m}_{Xe}$ is the xenon mass flow rate, U_d is the discharge voltage, I_d is the discharge current and P_{coils} is the power dissipated into solenoids [22]. Under standard operating conditions (300 V, $5.42\,\mathrm{mg\,s^{-1}}$), the SPT100-ML

engine delivers a thrust of 82 mN [4] and P_{coils} is typically 40 W. Thus the thrust efficiency reaches 44.6%. For modern HET, η_F lies between 45% and 65% [23]. In spite of a high efficiency, previous numbers reveal that a non-negligible fraction of the input power is not converted into thrust. Part of the applied power is transferred to the gas in the form of heat, i.e. random thermal motion, as well as internal energy by way of production of ionized and excited species [3, 4, 6]. Dispersion of the ion kinetic energy, which leads to a broadening of the ion velocity distribution function, and plasma beam divergence are other sources of power losses [20, 24]. Finally, a substantial part of the input power is lost onto the discharge channel walls through the process of plasma–surface interactions [25]. This loss channel is of special interest here since it governs the thermal state of Hall effect thrusters.

Inside a HET discharge chamber, plasma–surface interactions involve both ions and electrons, however in a different way. A thin non-neutral region is formed between the plasma and the wall, the so-called plasma sheath [26]. A fraction of ions created upstream in the channel are accelerated throughout this negative potential sheath. This fraction strongly depends upon the magnetic and electric field maps [6, 27]. They subsequently collide with the wall and transfer part of their energy to the bulk material. On the contrary, the sheath tends to repel electrons. In case of a non-conducting material like BN–SiO_2 and AlN ceramics, the flow of negative charge carriers balances the flow of positive charge carriers to the wall: there is no net current in the plasma sheath covering the floating wall [26]. Moreover, only a small fraction of electrons have enough energy to cross the sheath potential barrier and interact with the surface. The amount of energy fast electrons pass to the walls can at first sight be neglected. Heating of Hall thruster dielectric channel walls therefore mainly originates in ion bombardment. In addition, the high Xe^+ mass leads to an important momentum transfer to the wall, which in turn leads to wear of wall material by way of sputtering [6, 25]. As a matter of fact the ion flux to channel walls determines to a large extent the thruster lifetime. As can be seen in figure 4, the ion flow to the wall is largest in the final section of the channel, a region of high ion current since it corresponds to the zone through which ions are accelerated by the induced electric field [27]. As expected, see figure 4, the temperature gradient along the thruster channel wall increases with the input power.

On the basis of previous considerations, it is possible to estimate the power passed to the channel dielectric walls. As a first order approximation, one can consider the formation of an equilibrium collisionless sheath at the floating dielectric channel wall [26]. Indeed, full calculation of plasma sheath structure in a HET must account for non-maxwellian electrons, magnetic field and secondary electron emission [6]. Following the classical Debye layer approach, neglecting both the electron contribution and the ion thermal flux at the wall, the power P_{wall} deposited onto dielectric walls reads in W as

$$P_{\text{wall}} = j_{\text{i}} \left(\Delta\Phi + \alpha\Phi_{\text{i}} + \frac{3k_{\text{B}}T_{\text{i}}}{2\,e} \right) S_{\text{wall}}, \qquad (7)$$

$$\approx e\, n_{\text{e}}\, u_{\text{B}} \left(\Delta\Phi + \alpha\Phi_{\text{i}} + \frac{3k_{\text{B}}T_{\text{e}}}{2\,e} \right) S_{\text{wall}}, \qquad (8)$$

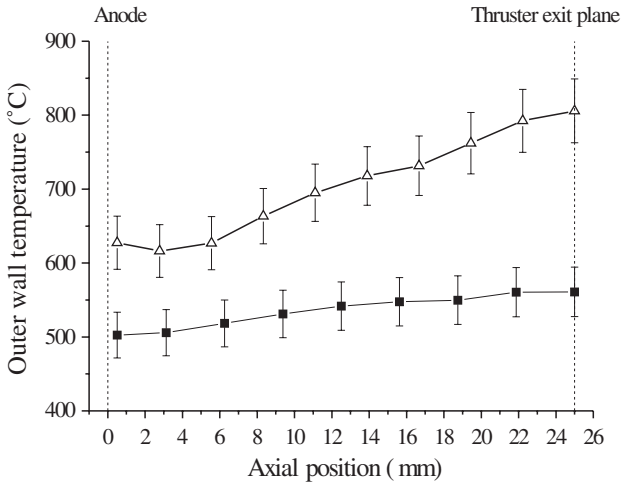

Figure 4. Temperature of the BN–SiO_2 channel outer wall of a SPT100-ML thruster for two input powers: 1370 W (■) and 2080 W (△). The axial temperature gradient is steeper at high input power.

where e is the elementary charge, k_{B} is Boltzmann's constant, j the current density, n the density, u_{B} the Bohm velocity, T the temperature, S the area and Φ refers to potential. Subscripts i and e refer to ions and electrons, respectively. Terms between brackets in fact represent kinetic, internal and thermal energy. In equation (8), $\Delta\Phi = \Phi_{\text{plasma}} - \Phi_{\text{wall}}$, which is the potential difference between the plasma medium and the floating wall, corresponds to the energy gained by an ion crossing the plasma sheath. Φ_{i} corresponds to the ionization potential and α is the accommodation factor, i.e. the fraction of internal energy actually given to the wall [27]. In equation (8), two further assumptions are made: charge neutrality, i.e. $n_{\text{e}} = n_{\text{i}}$, and temperature equilibrium $T_{\text{i}} \approx T_{\text{e}}$. Quantities like j_{i}, $\Delta\Phi$ and T_{e} have been measured by means of near-wall probes in the plasma sheath of the channel outer wall of a SPT100-like thruster [27]. Equation (8) can then be used to estimate power losses onto the BN–SiO_2 outer wall of a SPT100 thruster under standard operating conditions. For the final section of the wall ($l = 10$ mm), P_{wall} is equal to about 60 W.[6]

The case of the thruster anode is somewhat easier. Indeed, the anode, which is set at a high potential, mostly collects electrons. The ion contribution in heating of the anode can be neglected. The power lost by electrons is given by

$$P_{\text{anode}} = I_{\text{d}} \left(\Delta\Phi_{\text{a}} + \frac{3k_{\text{B}}T_{\text{e}}}{2e} \right) \approx I_{\text{d}} \left(\frac{5k_{\text{B}}T_{\text{e}}}{2e} \right), \qquad (9)$$

where $\Delta\Phi_{\text{a}}$ is the anode potential drop, with $\Delta\Phi_{\text{a}} \approx (k_{\text{B}}/e)\, T_{\text{e}}$. Electrons exhibit a relatively low temperature in the anode vicinity: $T_{\text{e}} \approx 5$ eV for a SPT100 HET under nominal conditions. Consequently, one finds $P_{\text{anode}} \approx 45$ W.

Previous numerical values are not to be taken as recommended values but only as indicative of a range. They clearly reveal that the power lost inside a HET channel represents several per cents of the applied electrical power. In the previous discussion, the role of multiply charged ions as well as UV radiations was disregarded. Multiply charged Xe^{n+} ions, especially Xe^{2+} ions, even if in the minority, might

[6] The following quantities were used in the calculation: $j_{\text{i}} = 35$ mA cm^{-2}, $\Delta\Phi = 30$ V, $\alpha = 0.7$, $T_{\text{e}} = 10$ eV.

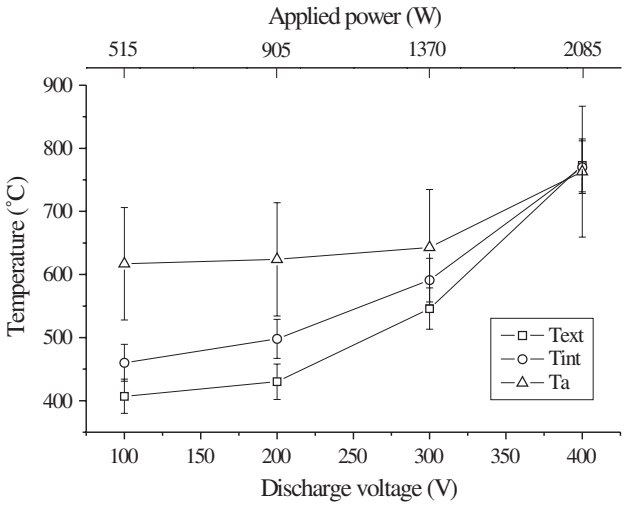

Figure 5. BN–SiO_2 channel wall and anode temperature of a SPT100-ML thruster as a function of applied voltage with a 5 mg s^{-1} xenon mass flow rate through the gas injector (anode). The coil current is fixed at 4.5 A.

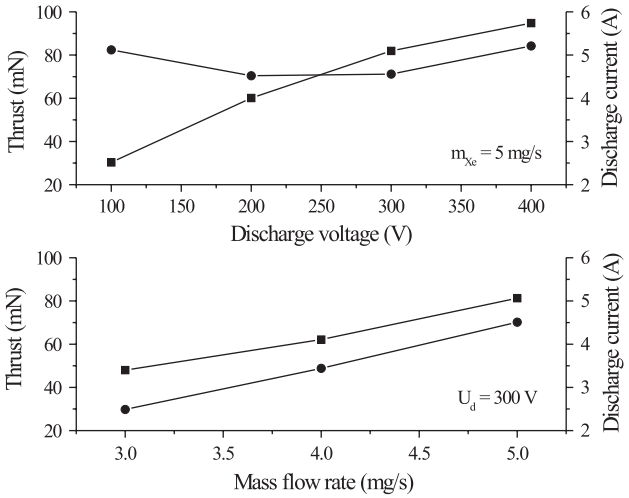

Figure 6. Thrust (■) and anode discharge current (●) for various applied voltages (above) and xenon mass flow rates (below). The error in thrust measurement is ±2% [4].

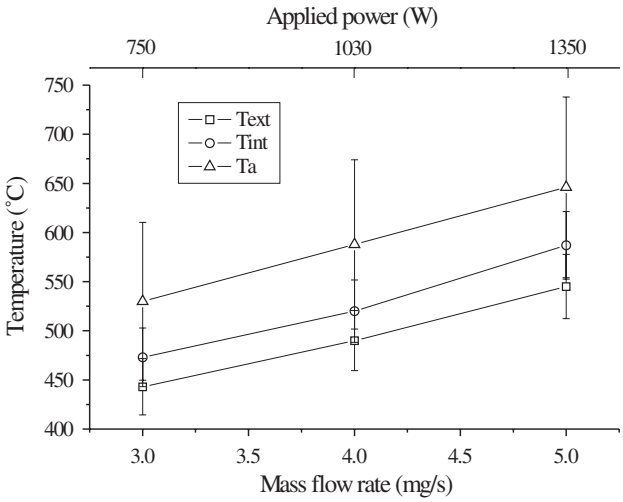

Figure 7. BN–SiO_2 channel wall and anode temperature as a function of supplied xenon mass flow rate at 300 V discharge voltage for a SPT100-ML thruster. The coil current is fixed at 4.5 A.

participate in power loss mechanisms inside the channel as they experience a stronger acceleration through the plasma sheath [6, 28]. It is worth noticing that the high thruster wall temperature is also due to the fact that the annular channel forms an enclosure in which thermal radiation trapping is favoured.

Atoms do not participate in a significant way in energy deposition processes. They drift slowly towards the channel exhaust and they are relatively cold. Moreover, most of them being in the electronic ground-state, the neutral flow carries away a negligible amount of internal energy. Nevertheless, it is interesting to note that the low gas density inside the thruster channel, i.e. long heavy particle collision mean free path, warrants thermal equilibrium between walls and gas temperature in the steady state [29]. Indeed, the mean thermal insulator temperature, which is around 550 °C at 1350 W input power for a SPT100 thruster, corresponds to the gas temperature. Emission spectroscopy measurements performed on N_2 molecules and N_2^+ molecular ions indicate that T_{gas} = (500±120) °C [11, 30]. Direct measurements of the xenon atom temperature by means of the Fabry–Pérot interferometry give $T_{gas} = (600 \pm 150)$ °C [31].

4.2. Influence of the thruster operating parameters

Figure 5 displays the temperature of SPT100-ML thruster components as a function of the applied voltage while keeping the mass flow rate injected through the anode fixed at 5 mg s^{-1}. The current flowing through coils is kept constant at 4.5 A meaning that the magnetic map is not adjusted to minimize I_d when changing U_d. In other words, the thruster is not optimized to get the highest thrust efficiency [4]. As can be seen in figure 6, the discharge current slightly varies around 4.8 A when changing the voltage from 100 to 400 V. The discharge current is not much affected unless the voltage is ramped up to a high value and the electron density even tends to decrease [3, 6, 7]. Yet, both the temperature of the anode and of the channel walls increase drastically with voltage, see figure 5. An increase in discharge voltage particularly leads to an increase in T_e as electrons gain energy through the potential drop. Note that at low voltage level the electron temperature rises linearly with the discharge voltage [32]. In the downstream part of the channel, the ion current towards the walls increases since the ion kinetic energy is linked to U_d. Thus the combination of these two effects explains the observed increase in outer and inner wall temperature, see figure 5. The anode temperature is directly linked to T_e, as shown in an indirect way in equation (9).

Figure 6 suggests that the thrust is proportional to $\sqrt{U_d}$ when keeping $\dot{m}_{Xe}$ at constant level. Indeed, $F \approx \dot{m}_{Xe^+} \times v$, where v is the Xe^+ ion final speed and $v \propto \sqrt{U_d}$ as observed from the Fabry–Pérot interferometry measurements [33].

The graph in figure 7 corresponds to the temperature of several thruster components as a function of the propellant mass flow supplied through the gas distributor, while the cathode mass flow rate is fixed. The applied voltage is kept constant at 300 V and the magnetic field is not modified. As

can be seen in figure 7, the temperature of all thruster elements is modified in a linear way as soon as the propellant mass flow is varied. The ionization efficiency being not much affected by a variation of the mass flow rate, the plasma density n_e follows changes of $\dot{m}_{Xe}$, as does the discharge current, see figure 6. According to equation (8), the power lost onto channel walls varies as n_e, hence the observed trend in ceramic wall temperature assuming that T_{wall} is proportional to P_{wall}. In a like manner, the increase in discharge current by way of n_e is directly responsible for the rise of the anode temperature, see figure 7.

As shown in figure 6, the thrust varies linearly with the injected xenon mass flow rate when keeping U_d fixed owing to the fact that $\dot{m}_{Xe^+}$ depends linearly upon $\dot{m}_{Xe}$ [4]. A more rigorous treatment of the problem, however, shall account for multiply charged ions.

Study of the influence of both the applied voltage and the injected propellant mass flow upon the thruster temperature field was also performed with a specific version of the SPT100-ML thruster equipped with a set of commercially available SmCo magnets instead of magnetic coils [19,34]. No trim coil was used meaning that optimization of thruster operation was not realized [3,7]. Similar results were found [19].

Figures 5 and 7 reveal that the steady state temperature of the SPT100 inner insulator wall T_{int} is higher than the temperature of the outer wall T_{ext}. Such a trend is predicted by thermal model and it has also been observed experimentally when measuring the temperature of a PPS®1350 thruster by means of thermocouples [8, 11]. It is indeed difficult for the internal thermal insulator to evacuate heat outwards due to its shape, its location, its relatively small area and the fact that it surrounds the central solenoid. Furthermore, the location of the ion production zone and the curvature of the electrostatic lens may lead to preferably point the ion beam at the inner wall [20]. Indeed, the magnetic field configuration has a strong impact on the temperature distribution inside the channel of a HET, as was reported in a preceding paper [19].

5. HET wall temperature in a broad range of power

5.1. Temperature to power ratio

In order to examine the effect of thruster working parameters on losses of power due to plasma–surface interactions, an interesting quantity to be studied is the channel wall temperature to power ratio R_{TP} in K/W defined as

$$R_{TP} = \frac{T_{wall}}{P} \qquad \text{with} \quad T_{wall} = \frac{T_{ext} + T_{int}}{2}. \tag{10}$$

In previous formula, T_{ext} is the mean external wall temperature and T_{int} is the mean internal wall temperature. The two temperatures are measured by means of infrared thermal imaging in steady state in the final section of the channel where most of the energy is lost, as shown in figure 4. The input power P is simply given by $U_d \times I_d$. Defined that way, R_{TP} allows to quantify, through its effect, the amount of power lost onto walls per unit input electrical power. In figure 8, R_{TP} is plotted as a function of applied power for three types of HET with similar channel dimensions: SPT100-ML with magnets, SPT100-ML with a magnetic coil assembly and PPS®1350-G. The thrusters

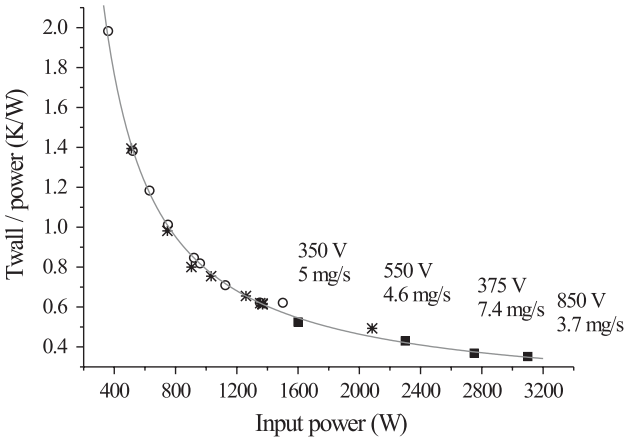

Figure 8. Ratio of the mean channel wall temperature to the power as a function of the applied power $I_d \times U_d$ for three Hall effect thrusters: SPT100-ML with magnets ○), SPT100-ML with solenoids (✳) and PPS®1350-G (■). Walls are made of BN–SiO_2 ceramic. Numbers are given fro the PPS®1350-G engine.

are all equipped with BN–SiO_2 dielectric walls. The SPT100-ML thruster with solenoids was not optimized whereas for the PPS®1350-G engine the current flowing through coils was varied to minimize I_d.

Two striking conclusions can be drawn from the graph in figure 8. First, R_{TP} varies in a smooth way over a broad range of applied power. Second, the R_{TP} values follow the same distribution law whatever the thruster. For a specific channel geometry and material, the decrease in R_{TP} with P indicates that the amount of power lost onto walls per unit of supplied power is certainly lower at the high power. It implies a better utilization of energy for ionization and/or acceleration purposes at the high power level. This experimental result agrees with the fact that for a given HET design the thrust efficiency tends to increase with the input power [13, 28]. Furthermore, the evolution of R_{TP} along with P tells us that the wall temperature, therefore the power losses, depends neither on thermal history of the thruster nor on material surface conditions nor on the magnetic field map as long as differences are not drastic. Each thruster has its own past, in terms of overall operating cycle. In addition, the two measurement series reported in figures 5 and 7 were recorded one after each other with no shutdown period. The two SPT100-ML thrusters were equipped with fresh dielectric channel walls whereas the inner and outer ceramic rings of the PPS®1350-G thruster were worn with grooves originating in anomalous erosion [25]. The magnetic field map of a SPT100 thruster differs from the one of a PPS®1350-G. Moreover, the latter was magnetically optimized.

In short, for a given thruster design and a given wall material, R_{TP} is mainly a function of P as long as the magnetic field is not too far from the optimum one. The observed trend has certainly some limits in terms of power range, as suggested by the values of R_{TP} at 1500 and 2080 W that seemingly depart from the proposed law, see figure 8.

5.2. Influence of material and dimensions

The above analysis reveals that, for a given geometry and wall material, the steady state thermal behaviour of a HET

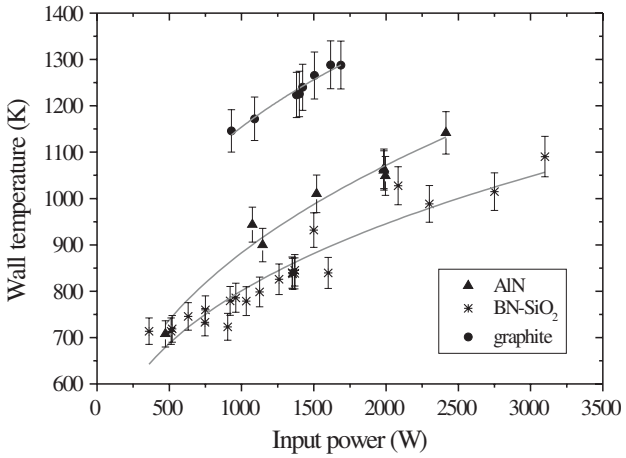

Figure 9. SPT100-ML thruster mean wall temperature as a function of applied power for three different materials: BN–SiO_2 (✳), AlN (▲) and graphite (●). Each solid line corresponds to a curve fitting based on a power law of the type $T_{wall} \propto P^n$, see table 2.

Table 2. Coefficients of the power law $T_{wall} = 270 + b \times P^n$ used to simulate the evolution of the mean channel wall temperature with the input power.

		b (K W^{-n})	n
SPT100-ML			
	BN–SiO_2	48 ± 9	0.35 ± 0.03
	AlN	43 ± 10	0.39 ± 0.03
	Graphite	138 ± 20	0.27 ± 0.02
PPSX000-ML			
	BN–SiO_2	32 ± 7	0.35 ± 0.03

depends principally upon the input power. Hence the interest in investigating the effect of both the material and the thruster design on channel wall temperature field. For argument's sake, instead of using the R_{TP} parameter we directly study the evolution of T_{wall} as a function of P.

Figure 9 displays the mean channel wall temperature as a function of the applied electrical power for a SPT100-ML thruster with a channel wall made of various materials: BN–SiO_2, AlN and graphite. Contrary to the first two compounds which are dielectric, graphite can conduct electricity, therefore leading to a different plasma discharge behaviour. The coil current was kept fixed at 4.5 A when using ceramics whereas it was varied from 3 to 5 A in the case of graphite walls. The discharge current depends upon the material properties as the latter determines plasma sheath properties and electron temperature [3, 4, 35]. The following values of I_d have been measured at 300 V applied voltage and 5 mg s^{-1} xenon mass flow rate: 4.5 A with BN–SiO_2, 6.5 A with AlN and and 5.7 A with graphite. The low value of I_d when using BN–SiO_2 explains both the high thruster efficiency and the reason why T_{BN-SiO_2} is the lowest whatever P, as can be seen in figure 9. In view of the discharge current magnitude, one would expect the channel wall temperature to be the highest with AlN. However, the SPT100 thruster is not suited to operate with conducting walls [4,35]. Indeed, when using graphite, the plasma potential map is such that the inner wall temperature is much greater than the outer wall temperature ($\Delta T \approx 400$ K), which explains the high value of $T_{graphite}$. As a matter of fact, results shown in figure 9 indicate that the material has a strong impact on

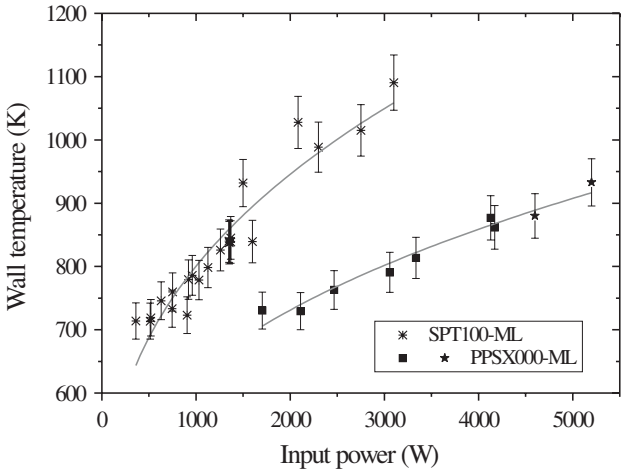

Figure 10. Evolution of the BN–SiO_2 dielectric wall temperature along with the applied power for thrusters having different dimensions: SPT100-ML (*) and PPSX000-ML (■, ✳). The latter is equipped with either a graphite anode (■) or with a stainless steel anode (✳). Each solid line corresponds to a curve fitting based on a power law of the type $T_{wall} \propto P^n$, see table 2.

T_{wall}. Material electric conductivity and secondary electron yield determine sheath properties, which in turn influence discharge behaviour. Moreover, thermodynamic coefficients like thermal diffusivity and emissivity drive the exhaust rate of heat.

According to data and curves in figure 9, T_{wall} always varies the same way with P whatever the channel wall material. In fact, the study of R_{TP} reported in section 5.1 already reveals that T_{wall} is a function of P. A statistical analysis indicates that the variation law can be written in the form

$$T_{wall} = a + b\, P^n. \tag{11}$$

The coefficient a represents the wall temperature when the thruster is not operated. In a vacuum chamber, one expects a to be close to room temperature: by means of thermal imaging we found a = 270 K. Coefficients b and n are given in table 2 for the three materials when keeping a at 270 K. These two coefficients characterize somehow power losses and thruster efficiency. For the two dielectric compounds, b and n do not differ much. However, the n number, which tells how strong is the dependence between T_{wall} and P, is slightly lower when BN–SiO_2 is employed, in agreement with the fact that BN–SiO_2 permits us to reach the highest engine performances. In the case of graphite, b is large and n is low that characterizes a poor thruster efficiency.

In figure 10, the average temperature of BN–SiO_2 ceramic walls is plotted as a function of the applied power for two thrusters having different dimensions. The channel diameter of the PPSX000-ML thruster is about 1.5 times the channel diameter of a SPT100-ML thruster [9]. Note that the PPSX000-ML thruster is always magnetically optimized when changing the operation conditions.

For a given input power, T_{wall} is much less for a PPSX000-ML HET that reveals the good thermal design of this high power thruster [9]. Radiators with optimized architecture have been added to the thruster. The thruster body and magnetic circuit are open to enable the outer dielectric wall to evacuate

most of its thermal power outwards without heating too much its surroundings. In such a way the amount of power stored in secondary heat sources like metal elements and coils is limited. Moreover, the low T_{wall} for the PPSX000-ML thruster in comparison with a SPT100-ML thruster also originates from the fact that the surface to volume ratio is higher for the former, which allows a better power loss distribution. Assuming that T_{wall} keep following the trend observed in figure 10 at high power, the mean wall temperature would reach 1100 K at 10 kW applied power, much below the BN–SiO_2 ceramic maximum sustainable temperature.

For the two thrusters, the mean wall temperature varies smoothly with the input power. In figure 10, a power law based on equation (11) is fitted to the two data sets with $a = 270$ K. Other coefficients are given in table 2. As expected, b is less for a large thruster. On the contrary, coefficient n is the same for the two HETs. It reveals that the value of n solely depends on the material and not on the discharge properties. During the measurement campaign, the PPSX000-ML thruster was equipped either with a graphite anode or with a stainless steel anode. As can be seen in figure 10, the evolution of T_{wall} does not depend upon the anode characteristics.

6. Conclusions

The investigation of the steady state temperature of a Hall effect thruster by means of calibrated infrared thermal imaging reveals a striking fact: the mean temperature of the thruster discharge chamber walls is mostly a function of the applied power, i.e. of the product of the current–voltage pair. Moreover, for a given thruster geometry and a given wall material, the temperature does not depend on the thruster thermal history, on the degree of wear and on the anode design. Besides, it depends weakly on the magnetic configuration. Such a simple trend is clearly in contradiction to the complexity of the plasma dynamics at work in a HET. This apparent contradiction might be solved in the case where physical processes occurring within the thin plasma sheath govern energy deposition mechanisms, being thus at the origin of this unexpected simple trend. The question is still open and it certainly needs further examination.

One way to get a better insight into plasma–surface interactions in a HET is to step forward. Instead of measuring the wall temperature, it is necessary to find a way to directly assess the flux of energy deposited by charged particles onto the discharge chamber walls. By comparing experimental outcomes with numerical simulations based on a hybrid model and with theoretical calculations accounting for the plasma sheath features, it might be possible to fully grasp the meaning of the relationship discovered in the course of these works.

Acknowledgments

This work is carried out in the frame of the research group CNRS/CNES/SNECMA/Universités 2759 ‘Propulsion Spatiale à Plasma’. P Lasgorceix and C Legentil are gratefully acknowledged for their skilful assistance and for providing us with complete sets of thruster working parameters. The authors would like to acknowledge fruitful discussions with M Prioul from Snecma Moteurs.

References

[1] Saccoccia G, Gonzalez del Amo J and Estublier D 2000 *ESA Bull.* vol 101
[2] Frisbee R H 2003 *J. Propul. Power* **19** 1129
[3] Zhurin V V, Kaufman H R and Robinson R S 1999 *Plasma Sources Sci. Technol.* **8** R1
[4] Gascon N, Dudeck M and Barral S 2003 *Phys. Plasmas* **10** 4123
[5] Koppel C R, Marchandise F, Prioul M, Estublier D and Darnon F 2005 The SMART-1 electric propulsion subsystem around the Moon: in flight experience *Proc. 41 Joint Propulsion Conf. and Exhibit (Tucson, AZ, USA)* AIAA paper 05-3671
[6] Morozov A I and Savelyev V V 2000 Fundamentals of stationary plasma thrusters theory *Rev. Plasma Phys.* **21** 203–391
[7] Kim V 1998 *J. Propul. Power* **14** 736
[8] Kim V, Kozlov V, Popov G, Skrylnikov A, Kozubsky K and Lyszyk M 1999 Investigation of the stationary plasma thruster outgassing and its thermal state impact on thruster performance variation in time *Proc. 26th Int. Electric Propulsion Conf. (Kitakyushu, Japan)* paper 84
[9] Duchemin O, Dumazert P, Clark S D and Mundy D H 2003 Development and testing of a high-power Hall thruster *Proc. 28th Int. Electric Propulsion Conf. (Toulouse, France)* paper 32
[10] Walter J and Dickens J 2001 Thermal characterization and modeling of a low-power laboratory model TAL *Proc. 27th Int. Electric Propulsion Conf. (Passadena, CA, USA)* paper 72
[11] Roche S, Barral S, Béchu S, Dudeck M, Lasgorceix P, Magne L, Minea T, Pagnon D and Touzeau M 1999 Thermal analysis of a stationary plasma thruster *Proc. 35th Joint Propulsion Conf. Exhibit (Los Angeles, CA, USA)* AIAA paper 99-2296
[12] Crofton M W, Uenten R H, Harris L, Yohnsee E M and Cohen R B 1996 Calibrated infrared imaging for electric thrusters, *Proc. 32nd Joint Propulsion Conf. and Exhibit (Lake Buena Vista, FL, USA)* AIAA paper 96-2977
[13] Vial V, Lazurenko A, Bouchoule A, Prioul M, Garrigues L and Boeuf J P 2004 PPS®1350-G in an extended operation domain: comparison between experimental and simulation results *Proc. 40th Joint Propulsion Conf. Exhibit (Fort Lauderdale, FL, USA)* AIAA paper 04-3607
[14] Wolfe W L and Zissis G J (ed) 1989 *The Infrared Handbook* (Ann Arbor, MI: Environmental Research Institute of Michigan)
[15] Siegel R and Howell J R 1992 *Thermal Radiation Heat Transfer* (Washington: Taylor and Francis)
[16] Rozenbaum O, De Sousa Meneses D, Chermanne S, Auger Y and Echegut P 1999 *Rev. Sci. Instrum.* **70** 4020
[17] *ThermaCAM SC 3000 Operator’s Manual* 1999 (FLIR systems AB, publ. no. 557 379)
[18] Jakob M 1958 *Heat Transfer* (New York: Wiley)
[19] Mazouffre S, Echegut P, Dubois F and Dudeck M 2004 Lessons learned from infrared thermal imaging of Hall effect thrusters *Proc. 4th Int. Spacecraft Propulsion Conf. (Sardinia)* (Noordwijk: ESA Publications Division) paper SP-555
[20] Vial V, Mazouffre S, Prioul M, Pagnon D and Bouchoule A 2005 *IEEE Trans. Plasma. Sci.* **33** 524
[21] Bouchoule A, Cadiou A, Héron A, Dudeck M and Lyszyk M 2001 *Contrib. Plasma Phys.* **41** 573
[22] Bouchoule A, Boeuf J P, Héron A and Duchemin O 2004 *Plasma Phys. Control. Fusion* **46** B407
[23] Lazurenko A, Vial V, Bouchoule A, Skrylnikov A, Kozlov V and Kim V 2006 *J. Propul. Power* **22** 38
[24] Dorval N, Bonnet J, Marque J P, Rosencher E, Chable S, Rogier F and Lasgorceix P 2002 *J. Appl. Phys.* **91** 4811
[25] Mazouffre S, Dubois F, Albarède L, Pagnon D, Touzeau M and Dudeck M 2003 Plasma induced erosion phenomena in a

Hall thruster *IEEE Proc. 03EX743, Recent Advances in Space Technologies* pp 56–61
[26] Lieberman M A and Lichtenberg A J 1994 *Principles of Plasma Discharges and Materials Processing* (New York: Wiley)
[27] Kim V *et al* 2005 Investigation of the local plasma parameters distributions in the SPT accelerating channel under increased discharge voltages *Proc. 29th Int. Electric Propulsion Conf. (Princeton, NJ, USA)* paper 04
[28] Lazurenko A, Vial V, Bouchoule A, Skrylnikov A, Kozlov V and Kim V 2006 *J. Propul. Power* **22** 38
[29] Bareilles J, Hagelaar G J M, Garrigues L, Boniface C and Boeuf J P 2004 *Phys. Plasmas* **11** 3035
[30] Bouchoule A *et al* 2001 *Plasma Sources Sci. Technol.* **10** 364
[31] Mazouffre S, Pagnon D, Lasgorceix P and Touzeau M 2003 Temperature of xenon atoms in a stationary plasma thruster *Proc. 28th Int. Electric Propulsion Conf. (Toulouse, France)* paper 283
[32] Raitses Y, Staack D, Keidar M and Fisch N J 2005 *Phys. Plasmas* **12** 057104
[33] Gawron D, Mazouffre S and Boniface C 2006 *Plasma Sources Sci. Technol.* **15** 757
[34] Renaudin P, Cagan V, Guyot M, Cadiou A, Lasgorceix P, Dudeck M, Vial V and Dumazert P 2003 Magnetic circuits for Hall thrusters: use of permanent magnets *Proc. 28th Int. Electric Propulsion Conf. (Toulouse, France)* paper 284
[35] Barral S, Makowski K, Peradzyński Z, Gascon N and Dudeck M 2003 *Phys. Plasmas* **10** 4137